

Performance characterization of a new temperature-robust gain-bandwidth improved MEMS gyroscope operated in air[☆]

Alexander A. Trusov^{*}, Adam R. Schofield, Andrei M. Shkel

MicroSystems Laboratory, Department of Mechanical and Aerospace Engineering, University of California, Irvine, Irvine, CA 92697-3975, USA

ARTICLE INFO

Article history:

Received 16 July 2008

Received in revised form

12 November 2008

Accepted 12 November 2008

Available online 24 November 2008

Keywords:

MEMS vibratory gyroscopes

Robust design

Random noise characterization

Allan variance

ARW

ARRW

ABSTRACT

This paper reports a new MEMS vibratory rate gyroscope designed with increased robustness to fabrication imperfections and variations in environmental conditions. The proposed architecture utilizes a single degree-of-freedom (DOF) drive-mode and a fully coupled 2-DOF sense-mode. The drive-mode operational frequency and the sense-mode bandwidth can be set independently, relaxing the tradeoff between the gain, die size, and detection capacitance inherent to the previously reported robust gyroscopes with dynamic vibration absorber (DVA) architecture of the 2-DOF sense-mode. Prototypes with 2.5 kHz operational frequency were extensively characterized in air and demonstrated sense-mode 3 dB bandwidth of 250 Hz. The uncompensated temperature coefficients of bias and scale factor were $313 (^{\circ}/\text{h})/^{\circ}\text{C}$ and $351 \text{ ppm }/^{\circ}\text{C}$, respectively. Using off-chip detection electronics, the rate sensitivity was $28 \mu\text{V}/(^{\circ}/\text{s})$, ARW – $0.09 (^{\circ}/\text{s})/\sqrt{\text{Hz}}$, bias instability – $0.08 (^{\circ}/\text{s})$, and ARRW – $0.03 (^{\circ}/\text{s})/\sqrt{\text{Hz}}$. Detailed time domain, Allan variance, and probability density function analysis revealed that both ARW and ARRW are of Gaussian type and Coriolis-uncorrelated, showing stable in-operational noise performance of the reported gyroscope.

© 2008 Elsevier B.V. All rights reserved.

1. Introduction

The operation of micromachined vibratory gyroscopes is based on a transfer of energy between two modes of vibration caused by the Coriolis effect [1]. Conventional implementations often utilize single degree-of-freedom (DOF) drive- and sense-modes [2,3]. In mode-matched implementations, the mechanical gain is proportional to the sense-mode quality factor, which allows increasing the sensitivity, theoretically without limit. However, the increase in quality factor of a mode-matched gyroscope is always at the cost of sensor robustness, temperature drift, bandwidth, and limited linear operational range. Also, precise matching of the operational modes over the operational temperature ranges defined by application requirements is practically challenging. Alternatively, the modes of operation can be designed with a certain frequency mismatch [2,3]. Even though this approach improves the robustness and bandwidth characteristics, the limitations of the structural design space (1-DOF drive and 1-DOF sense) dictate a tradeoff between achieved robustness/bandwidth and gain.

For increasing robustness of vibratory gyroscopes, it is beneficial to design 1-DOF drive- and 2-DOF sense-modes so that the drive-mode resonant frequency is placed between the two resonant peaks of the sense-mode. A design of a sense-mode with 2-DOF dynamic vibration absorber (DVA) architecture has been previously proposed and demonstrated to provide robust operation with a 200 Hz bandwidth using a micromachined prototype with a 750 Hz drive-mode operational frequency [4]. For this design concept, increasing the operational frequency would further increase the bandwidth, while also resulting in a decrease of the response gain. Adapting the DVA-based gyroscope design for operational frequencies above 1 kHz while maintaining the sense-mode peaks at a practical spacing is challenging due to the limitation of the structural design space and involves a stringent tradeoff between the die size and detection capacitance [5].

Most real-world applications, such as automotive, military, and consumer electronics, require robust yet sensitive gyroscopes with operational frequencies above several kHz in order to suppress the effect of environmental vibrational noise [6]. At the same time, the desired mechanical bandwidth of the sense-mode is typically above 100 Hz, but not more than 400 Hz [2,3].

Recently, a new architecture was introduced [7], which extends the design space of the previously reported gyroscopes with 2-DOF sense-modes and overcomes the limitations imposed by the DVA dynamics. In this paper, we present a more complete account of the new design and experimental characterization results. Section 2 introduces the new structural architecture of the robust gyroscope. Section 3 presents gain and bandwidth scaling advantages of

[☆] This paper is part of the Special Section of the Micromechanics Section of Sensors and Actuators based on contributions revised from the Technical Digest of the 2008 Solid-State Sensors, Actuators and Microsystems Workshop sponsored by the Transducer Research Foundation, Inc. (1–5 June 2008, Hilton Head Island, South Carolina, USA).

^{*} Corresponding author.

E-mail address: alex.trusov@gmail.com (A.A. Trusov).

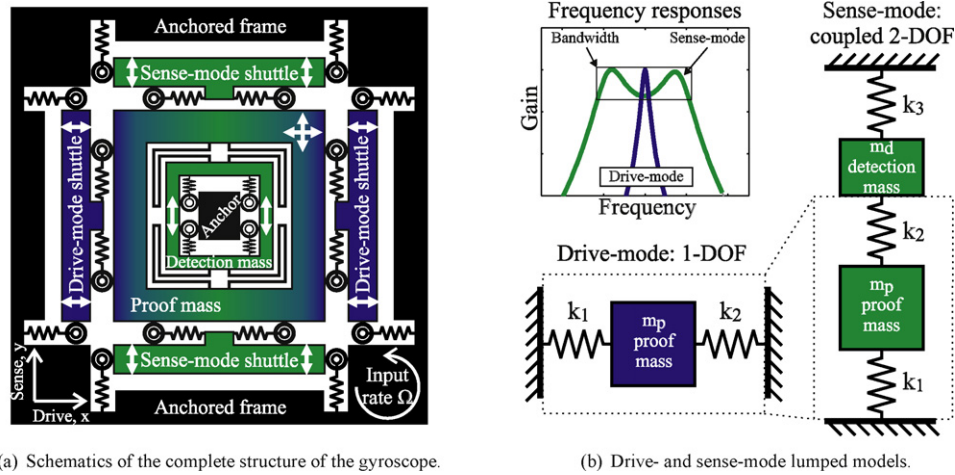


Fig. 1. General structural diagram of the proposed sensor element with a 1-DOF drive-mode and a fully coupled 2-DOF sense-mode: (a) schematics of the complete structure of the gyroscope and (b) drive- and sense-modes lumped models.

the proposed gyroscope architecture. Section 4 reports fabrication of the prototypes and their structural and thermal characterization. Section 5 describes in-depth experimental characterization of gyroscope's rate performance and rigorous analysis of random noise modes. Section 6 concludes the paper with a summary of results and conclusions.

2. Structural design and dynamics

2.1. Structural design

The structural implementation of the proposed gyroscope is shown in Fig. 1(a). It implements the novel fully coupled architecture shown in Fig. 1(b). The device consists of an anchored outer frame, two drive-mode and two sense-mode shuttles, a proof mass, a detection mass, and a central anchor. Each of the two drive-mode and two sense-mode shuttles is suspended relative to the fixed frame by two springs. These flexures restrict the motion of the shuttles to their respective axes. Similar suspension elements couple the four shuttles to the proof mass. The described configuration of 4 shuttles, 16 suspension elements, and a proof mass forms a symmetrically decoupled suspension. This suspension architecture was introduced in [8] and later adapted by several groups [9,10] for conventional vibratory gyroscopes with 1-DOF drive- and 1-DOF sense-modes. In this work, the conceptual architecture of the suspension is utilized in a gyroscope with a 2-DOF sense-mode for the first time.

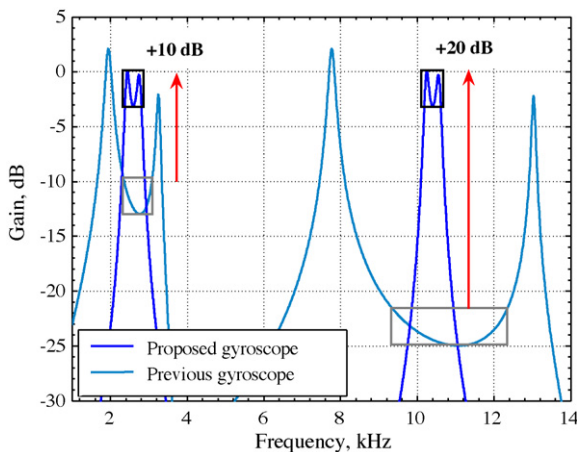


Fig. 2. Frequency scaling of the sense-mode frequency response of the proposed and DVA-based gyroscopes.

The proof mass m_p is suspended in the x - y plane with drive and sense stiffnesses of k_1 . Using the electrodes on the drive-mode shuttles, the mass is driven into drive-mode oscillation to form a Coriolis element sensitive to rotation along the z -axis. Unlike the conventional case [9,10], the Coriolis-induced motion is not directly picked-up from the proof mass, m_p , instead, the proof mass is coupled to a second, detection mass, m_d . The coupling flexure is bidirectional, with equal x and y stiffnesses k_2 . The detection mass is also coupled to the substrate with an inner suspension, k_3 . During rotation, the Coriolis acceleration of the proof mass is transferred to the detection mass, which responds in a wide frequency bandwidth due to the coupled dynamics of the proposed 2-DOF sense-mode.

Fig. 1(b) shows the lumped element drive and sense dynamic model of the proposed gyroscope. The drive-mode is a single-DOF system with mass m_p and stiffness $k_1 + k_2$. The sense-mode is a complete 2-DOF system, with two masses, m_p and m_d , and three stiffnesses $k_{1,2,3}$. The damping terms $c_{1,2,3}$ are located parallel to the respective spring elements.

2.2. Dynamics and selection of parameters

The drive-mode of the gyroscope is a single-DOF resonator with undamped natural frequency $\omega_n = \sqrt{(k_1 + k_2)/m_p}$. The sense-mode is a 2-DOF dynamic system with in-phase and anti-phase resonant modes. If the y -axis displacement of the proof mass is considered as the output of the system, the corresponding transfer function has a zero ("anti-resonance" condition) at the frequency $\omega_0 = \sqrt{(k_2 + k_3)/m_d}$. The proof mass anti-resonance is always located between the two sense-mode resonances and provides a convenient design guideline for selecting parameters of the system.

The available structural design parameters for the proposed gyroscope are the two masses $m_{p,d}$ and three stiffnesses $k_{1,2,3}$. These five parameters define the location of the drive-mode resonant frequency, i.e. the operational frequency of the gyroscope, and the locations of the two sense-mode resonant peaks which define the bandwidth of the gyroscope. In practice, the operational frequency and bandwidth requirements are dictated by the specific application. We denote the desired operational frequency by Φ and the sense-mode resonant peak spacing by $\Delta\Phi$. To ensure the optimal positioning of the drive-mode resonance with respect to the 2-DOF sense-mode response, we require that the drive-mode resonance coincides with the proof mass anti-resonance in the sense-mode.

We assume, that the masses of the gyroscope together with the capacitive electrodes are implemented first. Then, the three

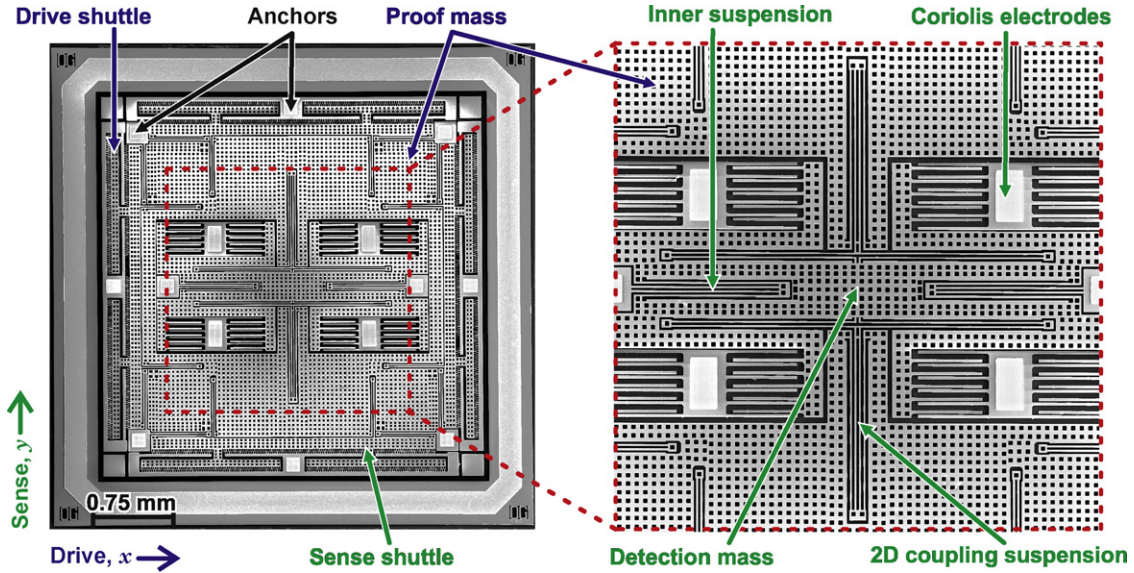


Fig. 3. SEM images of a fabricated MEMS gyroscope with 1-DOF drive-mode and a fully coupled 2-DOF sense-mode.

stiffnesses k_1 , k_2 , and k_3 become functions of the two masses m_p and m_d , and selection of the desired operational frequency Φ and the desired frequency spacing $\Delta\Phi$. According to [11], the system of three algebraic equations defining the stiffnesses of the proposed gyroscope design is

$$\begin{cases} \Phi^2 = \frac{k_1 + k_2}{m_p}, & \Phi^2 = \frac{k_2 + k_3}{m_d}, \\ \Delta\Phi = \sqrt{\Phi^2 + \sqrt{\frac{k_2^2}{m_p m_d}}} - \sqrt{\Phi^2 - \sqrt{\frac{k_2^2}{m_p m_d}}}. \end{cases} \quad (1)$$

Solving Eq. (1) for the three stiffnesses yields

$$\begin{cases} k_1 = m_p \Phi^2 - k_2, \\ k_2 = \Delta\Phi \sqrt{m_p m_d} \sqrt{\Phi^2 - \frac{\Delta\Phi^2}{4}}, \\ k_3 = m_d \Phi^2 - k_2. \end{cases} \quad (2)$$

The unique solution exists as long as $\Phi \geq \Delta\Phi/2$, which holds for any physically meaningful combination of the operational frequency and the frequency spacing.

For both the proposed gyroscope and the DVA-based design [4], the gain is inversely proportional to the sense-mode peak spacing. In the DVA-based design, however, the peak spacing cannot be adjusted freely without a sacrifice in detection capacitance and/or enlargement of the die due to the m_d/m_p mass ratio constraint [5]. This limitation is eliminated in the proposed device, where the peaks can be positioned arbitrary close to each other independent of the operational frequency and the mass ratio.

3. Gain and bandwidth modeling

Fig. 2 shows the effect of operational frequency scaling on the sense-mode frequency response for both the proposed and the DVA-based gyroscopes. Based on the parameters of the designed prototypes, we set the values of the proof and detection masses to $m_p = 4.72 \text{e} - 7 \text{ kg}$ and $m_d = 1.35 \text{e} - 7 \text{ kg}$. Assuming the device is operated in air, the damping coefficients are set to $c_1 = 1 \text{e} - 4 \text{ Ns/m}$, $c_2 = 5 \text{e} - 6 \text{ Ns/m}$, and $c_3 = 2 \text{e} - 4 \text{ Ns/m}$. For illustration purposes, the operational frequency is iterated between 2.6 kHz and 10.4 kHz, while the desired sense-mode frequency spacing is kept constant at 350 Hz. For the proposed gyroscope, the stiffnesses were obtained using Eq. (2).

The modeling confirms that the proposed design approach yields implementations with the prescribed operational frequency and that the sense-mode frequency spacing is independent of the proof and detection mass values. Due to the flexibility of the extended design space of the proposed gyroscope, the two peaks can be placed close together. In this case, the sense-mode response of the detection mass has an increased bandwidth, composed of the two coupled resonant peaks and the region in-between, while the gain is comparable to the mode-matched case. The described configuration is preferable for applications requiring operational frequencies in 2–20 kHz range and a bandwidth on the order of 100–350 Hz.

4. Structural characterization

4.1. Fabrication

The fabrication of prototypes was done using an in-house, wafer-level, two-mask process using SOI wafers with 50 μm thick device layer and 5 μm buried oxide layer. The first mask was used to define metallization of bonding pads using a lift-off process, while the second mask defined the structural layout. After patterning photoresist with the second mask, the wafers were subjected to a deep reactive ion etching (DRIE) using a Surface Technology Systems (STS) tool. Singulated dies were released in a HF acid bath. SEM images of a fabricated device are shown in Fig. 3.

4.2. Structural characterization

Experimental characterization of the lateral-comb device in atmospheric pressure is shown in Fig. 4. The measured drive-mode resonant frequency was 2.58 kHz which was located in-between the 2-DOF sense-mode resonances at 2.47 kHz and 2.73 kHz, and the drive-mode quality factor was 140. A 250 Hz 3 dB bandwidth was formed in the sense-mode by the two resonant peaks and the flat region in-between.

4.3. Thermal robustness

Temperature robustness, characterized by sensitivity of the bias and scale factor to temperature variations, is a critical performance parameter of gyroscopes targeted for real-world, temperature

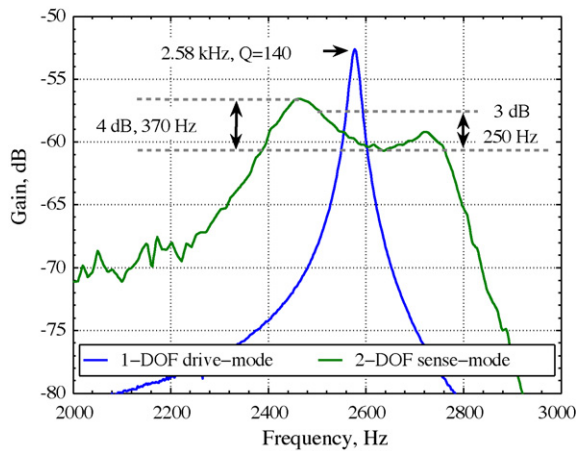


Fig. 4. Experimentally measured frequency responses of drive- and sense-modes of a fabricated prototype in air.

varying environments. The prototypes were experimentally characterized in variable temperature environment using a custom made, package-level heater equipped with a feed-back control, Fig. 5. Fig. 6(a) shows characterization of the temperature drifts of the single-DOF drive-mode operated in air. Increase in system temperature from 25 °C to 125 °C resulted in almost 2.5 dB drop in gain, yielding a temperature coefficient of approximately 3000 ppm/°C. Temperature coefficients of this order are typical in conventional gyroscopes with 1-DOF sense-modes.

Drive-mode temperature drifts are easily mitigated by closed loop operation. However, the drop of gain in the sense-mode can be detrimental to accuracy of conventional mode-matched gyroscopes. In the proposed gyroscope, the temperature drift of the sense-mode is minimized by using the 2-DOF structure.

Sense-mode frequency response of the detection mass was experimentally characterized at four different temperatures ranging from 25 °C to 125 °C, Fig. 6(b). Increase of temperature from 25 °C to 125 °C results in approximately 1 dB change of the gain in a 300 Hz bandwidth. The temperature change in the sense-mode gain evaluated at the corresponding drive-mode resonance frequency is approximately 0.3 dB over the 100 °C range. This yields the scale-factor temperature coefficient of 351 ppm/°C – approximately eight times improvement compared to the 1-DOF case. The temperature coefficient of the sense-mode phase was determined as 0.08°/°C.

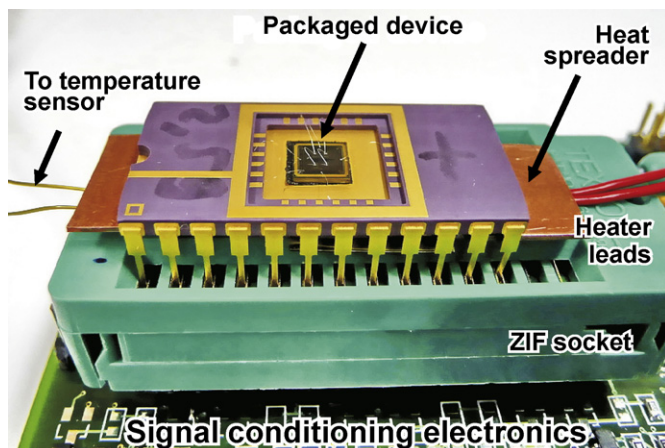
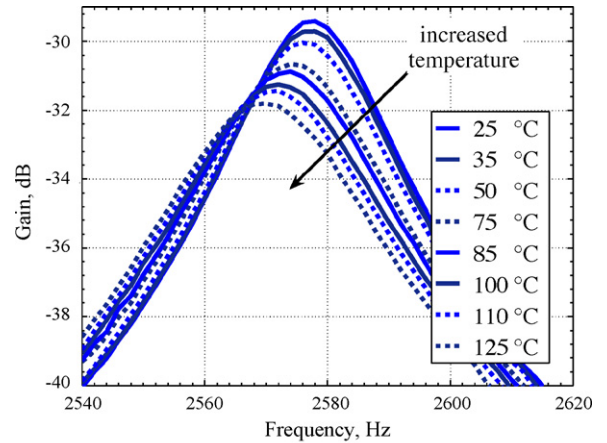
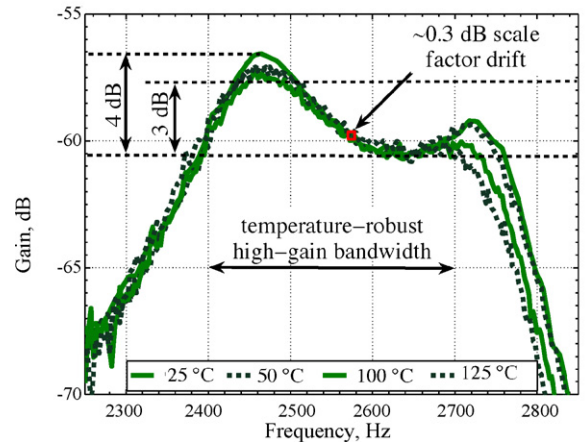


Fig. 5. Testbed for experimental characterization of temperature effects on the sensor response.



(a) 1-DOF drive-mode, temperature sensitivity ≈ 3000 ppm/°C



(b) 2-DOF sense-mode, temperature sensitivity ≈ 351 ppm/°C

Fig. 6. Comparison of the effect of temperature variations on the drive- and sense-modes in air: (a) 1-DOF drive-mode, temperature sensitivity ≈ 3000 ppm/°C and (b) 2-DOF sense-mode, temperature sensitivity ≈ 351 ppm/°C.

5. Rate and noise performance

5.1. Angular rate

The angular rate performance of the prototype was experimentally characterized in air using a computer-controlled Ideal Aerosmith 1291BR rate table. The electrical schematic of the experimental actuation and detection is shown in Fig. 7. The gyroscope was driven into 5 μ m peak-to-peak resonant motion using a combination of a 30 V DC bias and a 3.5 Vrms AC driving voltage applied to the anchored drive-mode lateral-comb electrode. An electro-mechanical amplitude modulation (EAM) technique [12] was used to detect the Coriolis-induced motion in the sense-mode. The AC carrier voltage with 3.5 Vrms amplitude at 20.5 kHz frequency was applied to the mobile masses; the anchored sense-mode parallel-plate electrode was connected to the inverting input of an operational amplifier, configured as a transimpedance amplifier [13].

Fig. 8 shows the calibration curve obtained by programming the rate table to constant angular rate motion and observing the corresponding voltage output of the gyroscope. The collected data-points were least squares fitted with a line to reveal a sensitivity of 28 μ V/(°/s). As only a single-sided capacitor was used, the total sensitivity of the device is 56 μ V/(°/s) for the same operational conditions. A 62.5°/s rate equivalent quadrature was measured by observing the out-of-phase output of the gyroscope at zero rate. The sensitivity and quadrature of the gyroscope are similar to the

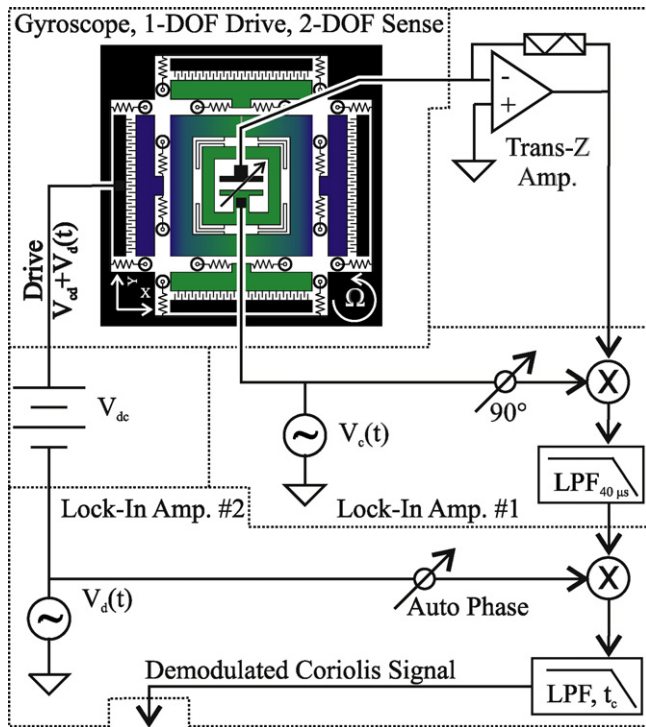


Fig. 7. Actuation and detection scheme used for the rate performance characterization based on EAM technique.

best performance numbers in MEMS gyroscopes operated in air reported in the literature [9,14].

From the structural characterization results above, the gyroscope's scale-factor temperature sensitivity was estimated as 351 ppm/°C. Based on the measured sense-mode phase temperature sensitivity and quadrature, the gyroscope's bias temperature sensitivity was estimated as 313 (°/h)/°C. Fig. 8 shows the rate response curves for −55 °C and 125 °C estimated using the measured bias and scale-factor temperature coefficients. The estimated maximum output drift over the 180 °C range is less than 5.4%, similar to the temperature-robustness level obtained in [4] using a lower resolution device operated at a sub-kHz frequency.

5.2. Random noise

Different random noise modes dominate the overall gyroscope noise level depending on the averaging time, which in its turn defines the useful sensor bandwidth [15,16]. The Allan variance method allows to identify random noise modes with different autocorrelation properties and their averaging time domain behavior [17]. For a given averaging time τ , Allan variance $\sigma_{AVAR}^2(\tau)$ is defined as one-half of the time average of the squares of the differences between successive readings sampled over the averaging time [18]. Random noise modes in output of MEMS rate sensors are typically uncorrelated and dominate over different time clusters, which allows to decouple and identify them using Allan variance (AVAR) analysis [15]. An Allan variance plot shows information given by power spectral density (PSD) of a measured data time history in an alternative and somewhat more convenient way. Specifically, $\sigma_{AVAR}(\tau) \propto \tau^\beta$ is equivalent to $PSD(f) \propto f^\alpha$, where $f = 1/\tau$ and $\beta = -(\alpha + 1/2)$ [19–22].

In general, high-frequency noises and white noise are reduced with longer averaging, i.e. $\sigma_{AVAR}(\tau)$ is a monotonically decreasing function of τ [17,18]. These noises can be suppressed at the cost of limiting the sensor bandwidth to lower frequencies. For $1/f$ type noise $\sigma_{AVAR}(\tau)$ is constant, i.e. its value is invariant to the averaging

time. For lower frequency fractional noises, such as $1/f^2$ noise, $\sigma_{AVAR}(\tau)$ is a monotonically increasing function; averaging signals with strong low-frequency noises is in fact detrimental to the overall quality of the measurement.

Fig. 9 shows characterization and analysis of the noise modes in the gyroscope's zero rate output (ZRO) in both the time and root Allan variance (RAVAR) domains. Fig. 9(a) shows the raw ZRO of the gyroscope captured at 100 Hz sampling rate, and its filtered versions; the nature of the applied filtering is clarified by the RAVAR analysis.

In the RAVAR Fig. 9(b) the measurement noise below 5e – 2 s is suppressed by the low-pass filter of the electronics. The measured angle random walk (ARW) is 0.09 (°/s)/√Hz. This white noise type random process dominates the measurement error in the range from 5e – 2 s to 3 s. The angle rate random walk (ARRW) or the random walk is 0.03 (°/s) √Hz. This random walk type process together with other lower-frequency fractional noises dominates the measurement error at averaging time above 5 s. The bias instability, defined as the minimum value of the $\sigma_{AVAR}(\tau)$ is 0.08 (°/s). The averaging time of 3–4 s associated with the bias instability point indicates the crossover time between two main random noise modes: rate white noise (or angle random walk, ARW) and rate random walk (angle rate random walk, ARRW).

Based on the identified critical time constants of the different random noise modes of the ZRO, it is possible to set frequency domain filters that separate a particular random noise mode. In Fig. 9(a) the measured output of the gyroscope was low-pass (LP), high-pass (HP), and band-pass (BP) filtered (F) with respect to the white noise versus random walk crossover frequency of 0.3 Hz. As expected, typical white noise (for HPF and BPF) and random walk (for LPF) type processes emerge in time domain from the total ZRO as the result of appropriate frequency-based filtering.

Complete characterization of the noise modes is essential for signal processing and noise performance optimization, however, the autocorrelation properties, exposed by the power spectral or Allan variance analyses do not define a random process completely. For instance, ARW, identified as the white noise component of the rate gyroscope output, can potentially have probability distribution function (PDF) different from Gaussian. The time history data from Fig. 9(a) was used to build empirical histograms, Fig. 10, which were checked against best-fit Gaussian PDFs. As Fig. 10(a) shows, the white noise ARW empirical PDF is close to Gaussian, suggesting it is indeed normally distributed. To check the probability distribution of the ARRW, we obtained its underlying white noise random process by differentiating ARRW with respect to time;

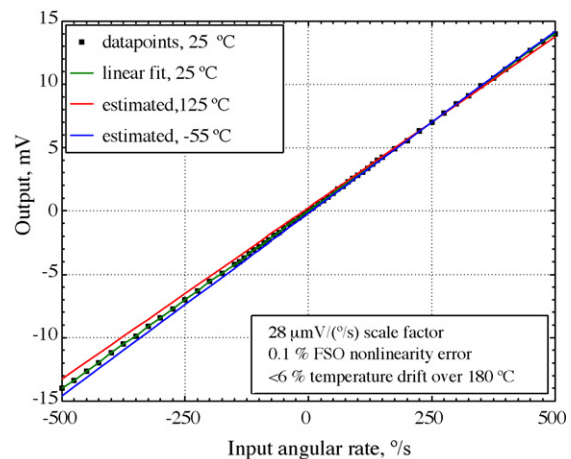
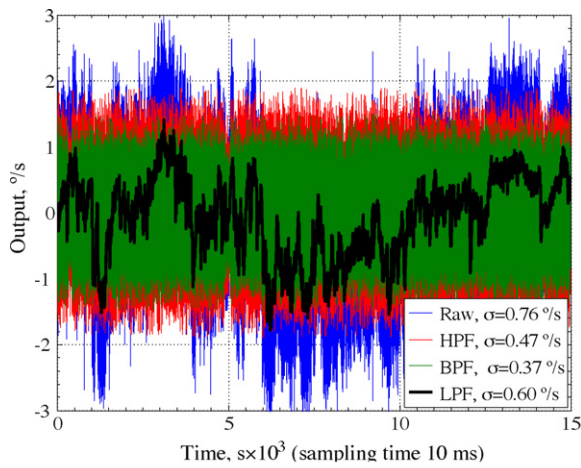
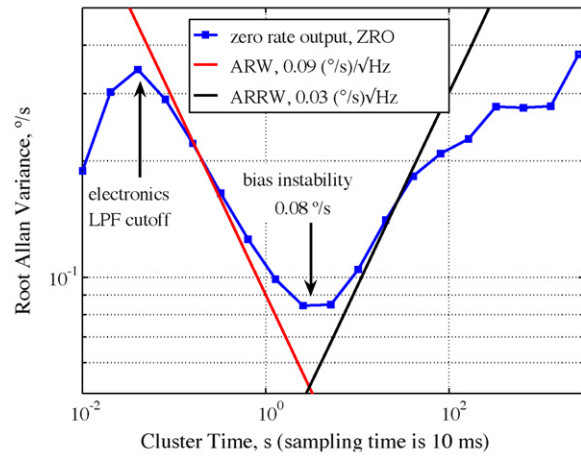


Fig. 8. Calibration rate plot, showing the measured relationship between angular rate input and the sensor voltage output.

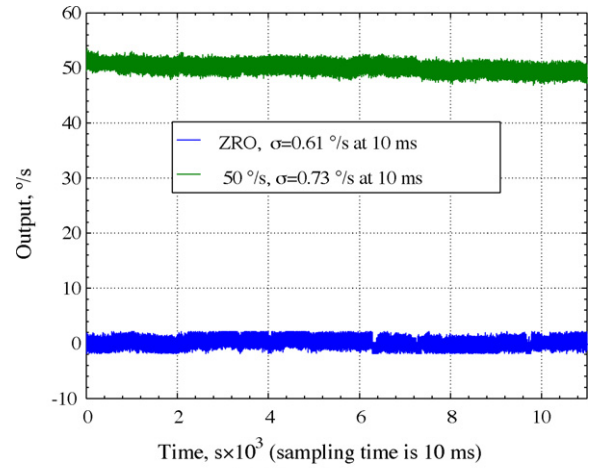


(a) Time history of the raw and the filtered data.

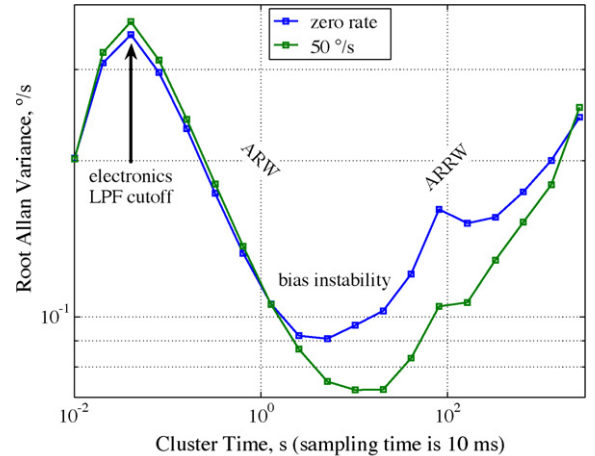


(b) Root Allan variance of the raw output.

Fig. 9. Identification of ZRO random noise modes using root Allan variance and frequency-based filtering of the time-domain signals: ARW is extracted by HPF, while ARRW is extracted by LPF: (a) time history of the raw and the filtered data and (b) root Allan variance of the raw output.

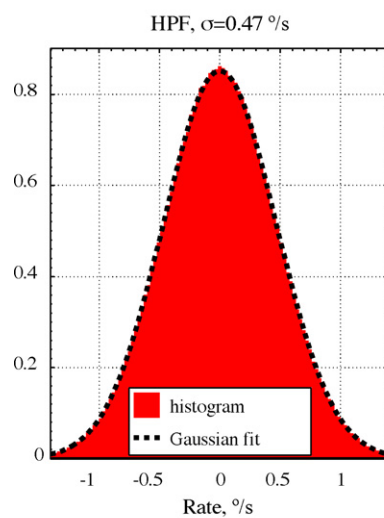


(a) Time history.

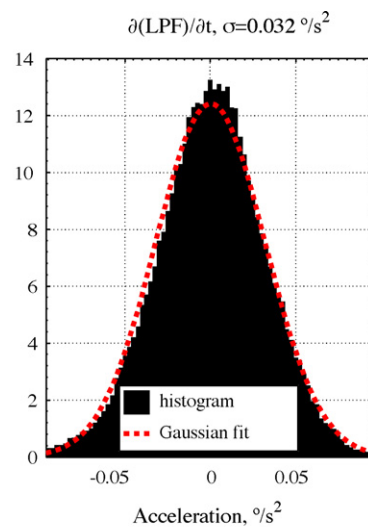


(b) Root Allan Variance.

Fig. 11. Comparative experimental study of noise at ZRO and 50°/s indicates good in-operation performance of the gyroscope: (a) time history and (b) root Allan variance.



(a) ARW (HPF of ZRO).



(b) ARRW (LPF of ZRO).

Fig. 10. Analysis of the empirical ARRW and ARW of the zero rate output shows Gaussian PDF (sampling time is 10 ms): (a) ARW (HPF of ZRO) and (b) ARRW (LPF of ZRO).

this process also appears to have Gaussian probability distribution, Fig. 10(b).

Random noise performance of vibratory MEMS gyroscopes is often characterized using ZRO data, e.g. [23,24,9,25,17]. Applying spectral density or Allan variance analyses to a gyroscope's zero input rate output provides valuable performance specifications but assumes the noise is not correlated with the Coriolis input; these methods may not be able to reliably predict noise performance of a gyroscope during actual operation when a non-zero input angular rate is applied. Fig. 11 compares noise performance of the gyroscope at zero rate and at a constant $50^\circ/\text{s}$ rate rotation. During the rotation, the ARW remained at approximately the same level, while the ARRW and the bias drifts slightly improved within the statistical bounds. These results indicate that the random noises in the gyroscope's output are additive and Coriolis-uncorrelated, leading to steady in-operation noise performance of the gyroscope.

6. Conclusions

We presented a novel gyroscope design which utilizes a 1-DOF drive-mode and a fully coupled 2-DOF sense-mode, comprising two masses with three suspension elements. To achieve optimal gain-bandwidth characteristics, the sense-mode bandwidth is defined by the two resonant peaks and the frequency region in-between. Due to the symmetry of the structure, the operational frequency is optimally placed between the sense-mode peaks even in presence of fabrication imperfections.

The gyroscope provides increased bandwidth as well as excellent robustness to fabrication imperfections. The temperature robustness of the reported prototype is on par with commercial quartz tuning fork devices [6,2] and superior to most commercial silicon gyroscopes [23,2].

The noise performance numbers of the reported gyroscope are comparable to performance of best conventional gyroscopes operated in air [23,9], despite the crude, non-differential, shelf-top electronics setup. Since a non-differential EAM method was used for detection, the rate equivalent noise performance is expected to improve at least an order of magnitude upon employment of a complete differential detection scheme where suppression of the carrier boosts the dynamic range [14]. Detailed Allan variance and probability density function analysis showed that both ARW and ARRW are of Gaussian type and Coriolis-uncorrelated, revealing stable in-operational noise performance of the reported gyroscope.

Acknowledgements

This work was supported by the Custom Sensors & Technologies Systron Donner Automotive (CS&T SDA, formerly BEI Technologies) contract BEI-36974, UC Discovery program ELE04-10202, and National Science Foundation Grant CMS-0409923. The gyroscopes were designed and characterized at the University of California, Irvine MicroSystems Laboratory. We would like to acknowledge the Integrated Nanosystems Research Facility (INRF) at UCI for the help with fabrication. We would also like to acknowledge Cenk Acar and Lynn E. Costlow of CS&T SDA for stimulating discussions.

References

- [1] A. Shkel, Type I and Type II micromachined vibratory gyroscopes, in: Proceedings of the IEEE/ION Position, Location, and Navigation Symposium, 2006, pp. 586–593.
- [2] M. Weinberg, A. Kourepenis, Error sources in in-plane silicon tuning-fork MEMS gyroscopes, *Journal of Microelectromechanical Systems* 15 (3) (2006) 479–491.
- [3] N. Yazdi, F. Ayazi, K. Najafi, Micromachined inertial sensors, *Proceedings of the IEEE* 86 (8) (1998) 1640–1659.
- [4] C. Acar, A. Shkel, Inherently robust micromachined gyroscopes with 2-DOF sense-mode oscillator, *IEEE Journal of Microelectromechanical Systems* 15 (2) (2006) 380–387.
- [5] A.R. Schofield, A.A. Trusov, A.M. Shkel, Effects of operational frequency scaling in multi-degree of freedom MEMS gyroscopes, *IEEE Sensors Journal* 8 (10) (2008) 1672–1680.
- [6] A. Madni, L. Costlow, S. Knowles, Common design techniques for BEI gyrochip quartz rate sensors for both automotive and aerospace/defense markets, *IEEE Sensors Journal* 3 (5) (2003) 569–578.
- [7] A.A. Trusov, A.R. Schofield, A.M. Shkel, New architectural design of a temperature robust MEMS gyroscope with improved gain-bandwidth characteristics, in: Proceedings of a Solid-State Sensors, Actuators and Microsystems Workshop (Hilton Head Workshop 2008), 2008, pp. 14–17.
- [8] M.S. Kranz, G.K. Fedder, Micromechanical vibratory rate gyroscope fabricated in conventional CMOS, in: Symposium Gyro Technology, Stuttgart, Germany, September 16–17, 1997, pp. 3.0–38.38.
- [9] S. Alper, K. Azgin, T. Akin, A high-performance silicon-on-insulator MEMS gyroscope operating at atmospheric pressure, *Sensors and Actuators A: Physical* 135 (2006) 34–42.
- [10] J.G.L. Woon-Tahk Sung, S. Sung, T. Kang, Design and performance test of a MEMS vibratory gyroscope with a novel agc force rebalance control, *IOP Journal of Micromechanics and Microengineering* 17 (10) (2007) 1939–1948.
- [11] J.P.D. Hartog, *Mechanical Vibrations*, Dover Publications, 1985.
- [12] A.A. Trusov, A.M. Shkel, Capacitive detection in resonant MEMS with arbitrary amplitude of motion, *IOP Journal of Micromechanics and Microengineering* 17 (8) (2007) 1583–1592.
- [13] P. Horowitz, W. Hill, *The Art of Electronics*, Cambridge University Press, 1989.
- [14] A.A. Trusov, I. Chepurko, A.R. Schofield, A.M. Shkel, A standalone programmable signal processing unit for versatile characterization of MEMS gyroscopes, in: IEEE Sensors Conference, Atlanta, GA, USA, October 28–31, 2007.
- [15] IEEE standard specification format guide and test procedure for single-axis interferometric fiber optic gyros, *IEEE Std* 952, 1997.
- [16] IEEE standard specification format guide and test procedure for coriolis vibratory gyros, *IEEE Std* 1431, 2004.
- [17] R. Neul, U.-M. Gomez, K. Kehr, W. Bauer, J. Classen, C. Doring, E. Esch, S. Gotz, J. Hauer, B. Kuhlmann, C. Lang, M. Veith, R. Willig, Micromachined angular rate sensors for automotive applications, *IEEE Sensors Journal* 7 (2) (2007) 302–309.
- [18] N. El-Sheimy, H. Hou, X. Niu, Analysis and modeling of inertial sensors using allan variance, *IEEE Transactions on Instrumentation and Measurement* 57 (1) (2008) 140–149.
- [19] E. Masry, Flicker noise and the estimation of the allan variance, *IEEE Transactions on Information Theory* 37 (4) (1991) 1173–1177.
- [20] G. Wei, Flicker noise process analysis, in: Proceedings of the 47th IEEE International Frequency Control Symposium, 1993, pp. 321–325.
- [21] C. Greenhall, Does Allan variance determine the spectrum? in: Proceedings of the IEEE International Frequency Control Symposium, 1997, pp. 358–365.
- [22] C. Greenhall, Spectral ambiguity of allan variance *IEEE Transactions on Instrumentation and Measurement* 47 (3) (1998) 623–627.
- [23] J. Geen, S. Sherman, J. Chang, S. Lewis, Single-chip surface micromachined integrated gyroscope with 50 deg/h Allan deviation, *IEEE Journal of Solid-State Circuits* 37 (12) (2002) 1860–1866.
- [24] J.-Y. Lee, S.-H. Jeon, H.-K. Jung, H.-K. Chang, Y.-K. Kim, Vacuum packaged low noise gyroscope with sub mdeg/s/root-hz resolution, in: Proceedings of the 18th IEEE International Conference on Micro Electro Mechanical Systems MEMS 2005, 2005, pp. 359–362.
- [25] A. Sharma, M. Zaman, F. Ayazi, A smart angular rate sensor system, in: Proceedings of the IEEE Sensors 2007 Conference, Atlanta, GA, USA, October 28–31, 2007.